Emergent topological spin structures in the centrosymmetric cubic perovskite SrFeO_{3}

S. Ishiwata, T. Nakajima, J.-H. Kim, D. S. Inosov, N. Kanazawa, J. S. White, J. L. Gavilano, R. Georgii, K. M. Seemann, G. Brandl, P. Manuel, D. D. Khalyavin, S. Seki, Y. Tokunaga, M. Kinoshita, Y. W. Long, Y. Kaneko, Y. Taguchi, T. Arima, B. Keimer, and Y. Tokura

Phys. Rev. B **101**, 134406 — Published 6 April 2020
DOI: 10.1103/PhysRevB.101.134406

Emergent topological spin structures in centrosymmetric cubic perovskite $SrFeO_3$

S. Ishiwata,[1, 2, 3, *] T. Nakajima,[4] J. -H. Kim,[5] D. S. Inosov,[5, 6] N. Kanazawa,[1]
J. S. White,[7] J. L. Gavilano,[7] R. Georgii,[8, 9] K. M. Seemann,[8, 9] G. Brandl,[9] P.
Manuel,[10] D. D. Khalyavin,[10] S. Seki,[4] Y. Tokunaga,[11] M. Kinoshita,[1] Y. W.
Long,[4, 12] Y. Kaneko,[4] Y. Taguchi,[4] T. Arima,[4, 11] B. Keimer,[5] and Y. Tokura[1, 4]

[1]*Department of Applied Physics and Quantum-Phase Electronics Center (QPEC),*
University of Tokyo, Hongo, Tokyo 113-8656, Japan
[2]*JST-PRESTO, Kawaguchi, Saitama 332-0012, Japan*
[3]*Division of Materials Physics, Graduate School of Engineering Science,*
Osaka University, Toyonaka, Osaka 560-8531, Japan
[4]*RIKEN Center for Emergent Matter Science (CEMS), Wako, Saitama 351-0198, Japan*
[5]*Max-Planck-Institut für Festkörperforschung, D-70569 Stuttgart, Germany*
[6]*Institut für Festkörper- und Materialphysik,*
TU Dresden, 01069 Dresden, Germany
[7]*Laboratory for Neutron Scattering and Imaging (LNS),*
Paul Scherrer Institut (PSI), CH-5232 Villigen, Switzerland
[8]*Physik Department E21, Technische Universität München, D-85748 Garching, Germany*
[9]*Heinz Maier-Leibnitz Zentrum (MLZ),*
Technische Universität München, D-85748 Garching, Germany
[10]*ISIS Facility, STFC Rutherford Appleton Laboratory,*
Chilton, Didcot, Oxfordshire, OX11 0QX, United Kingdom
[11]*Department of Advanced Materials Science,*
University of Tokyo, Kashiwa 277-8561, Japan
[12]*Beijing National Laboratory for Condensed Matter Physics,*
Institute of Physics, Chinese Academy of Sciences, Beijing 100190, China

(Dated: February 28, 2020)

Abstract

The skyrmion crystal (SkX) characterized by a triple-$\boldsymbol{q}$ helical spin modulation has been reported as a unique topological state that competes with the single-$\boldsymbol{q}$ helimagnetic order in noncentrosymmetric materials with Dzyaloshinskii-Moriya (DM) interactions. Here we report the discovery of a rich variety of multiple-$\boldsymbol{q}$ helimagnetic spin structures in the centrosymmetric cubic perovskite $SrFeO_3$ without DM interactions. On the basis of neutron diffraction measurements, we have identified two types of robust multiple-$\boldsymbol{q}$ spin structures that appear in the absence of external magnetic fields: an anisotropic double-$\boldsymbol{q}$ spin spiral and an isotropic quadruple-$\boldsymbol{q}$ spiral hosting a three-dimensional lattice of topological singularities. The present system not only diversifies the family of SkX host materials, but furthermore provides an experimental missing link between centrosymmetric lattices and topological helimagnetic order. It also offers perspectives for integration of SkXs into oxide electronic devices.

PACS numbers: 75.25.-j, 75.30.-m, 75.30.Kz

---

[*] Electronic address: `ishiwata@mp.es.osaka-u.ac.jp`

I. INTRODUCTION

The discovery of novel magnetic structures has the potential to open new fields in condensed matter physics. This is exemplified by magnetic skyrmions with a vortex-like spin configuration, which has led to a multitude of possible applications of topological spin textures in spintronics [1–5]. Highly symmetric crystal lattices allow magnetically ordered states with different equivalent propagation vectors $\boldsymbol{q}$, and complex mesoscopic superstructures can emerge from superpositions of several such degenerate states. The ”skyrmion crystal” (SkX), viewed as a multi-$\boldsymbol{q}$ superposition of magnetic skyrmions spin helices, has garnered particular recent attention because of its intriguing connection to topological spin and charge transport phenomena [6–9].

So far, SkXs have mostly been reported for non-centrosymmetric lattices, with details depending on the symmetry of the underlying crystal lattice, the magnetic anisotropy, and the relative strength of the competing interactions; i.e., the ferromagnetic exchange interaction and the Dzyaloshinskii-Moriya (DM) interaction [5]. Three types of two-dimensional SkX characterized by multiple coplanar $\boldsymbol{q}$ vectors have been reported: (i) a Bloch-type SkX formed by superposing three proper-screw spin modulations, which has been found in chiral helimagnets such as B20 compounds (MnSi, FeGe, etc.)[3, 10–12], Cu_2OSeO_3[13], and Co-Zn-Mn alloys [14], (ii) a Néel-type SkX formed by three cycloidal spin modulations found in polar helimagnets, like $GaV_4(S,Se)_8$ and $VOSe_2O_5$[15–18], and (iii) an antiskyrmion crystal formed by three spiral spin modulations found in a Mn-Pt-Sn inverse Heusler compound with $D2d$ symmetry [19]. Note that the DM interaction induced at a surface or interface can stabilize the Néel-type SkX as seen in a Fe monolayer on Ir(111) surface [20]. Recently, a three-dimensional topological spin structure generated by triple-$\boldsymbol{q}$ vectors that are orthogonal to each other has been identified in the B20 compound MnGe with the DM interaction [21]. This spin structure has hedgehog and antihedgehog singularities as bridged by intervening skyrmion strings, where the associated emergent magnetic monopole and antimonopole manifest themselves as a source of anomalous magnetotransport phenomena [7, 22].

In noncentrosymmetric helimagnets, the DM interaction originating from spin-orbit coupling apparently plays an important role in the formation of a SkX by selecting both the helicity and vorticity for each skyrmion [7, 21, 22]. On the other hand, the emergence of SkXs has been theoretically predicted also to occur in centrosymmetric helimagnets with high lattice symmetry [23–28]. In the absence of the DM interaction, these helimagnets have the potential to show rich topological spin textures due to fewer constraints on the spin helix. There exist a large number of centrosymmetric helimagnets, some of which show multiple-$\boldsymbol{q}$ spin modulations such as the rare-earth magnets [29, 30]. However, the presence of topologically nontrivial helimagnetic phases in centrosymmetric systems remains to be explored.

The simple cubic perovskite $SrFeO_3$ with crystal structure displayed in Fig. 1(a) is known to host a helimagnetic order below 130 K with metallic conductivity [31, 32]. The origin of the helimagnetic order in $SrFeO_3$ and related iron oxides has been discussed in terms of the competing exchange interactions, i.e., the nearest-neighbor and the further-neighbor interactions [33] or the double-exchange mechanism considering the itinerant oxygen p holes [34, 35]. Early neutron diffraction data were described in terms of a single-$\boldsymbol{q}$ proper-screw spiral with propagation vector along [111] or equivalent directions of the cubic lattice [32]. Recently, however, $SrFeO_3$ was shown to display a rich variety of helimagnetic phases depending on temperature and external magnetic field as shown in Fig. 1(a) [36, 37]. Among them, Phases I and II are extraordinary in the sense that they exhibit a large unconventional Hall effect [36, 38, 39]. The presence of sharp phase transitions with unusual transport signatures indicates well-ordered magnetic superstructures, rather than an incoherent superposition of domains of the single-$\boldsymbol{q}$ structure with different propagation vectors. In both Phase I and Phase II, the Hall resistivity as a function of $\boldsymbol{H}$ along [111] increases nonlinearly and reaches a maximum below the phase boundary to Phase IV or Phase V. While this behavior implies the emergence of noncoplanar and/or topological spin textures with scalar spin chirality [6, 7], the magnetic structures within each phase have remained elusive. In this work, on the basis of comprehensive single crystal neutron diffraction studies, we reveal that the magnetic structures of the mysterious phases in the centrosymmetric cubic perovskite $SrFeO_3$ can be topological in nature, being identified as anisotropic double-$\boldsymbol{q}$ and isotropic quadruple-$\boldsymbol{q}$ helimagnetic structures, respectively.

II. EXPERIMENTAL

Single crystals of $SrFeO_3$ and $SrFe_{0.99}Co_{0.01}O_3$ were obtained by a high-pressure oxygen annealing for the large single crystals of the oxygen-deficient perovskite with brownmilleritetype structure as described in Refs. [36] and [40]. The orientation of the single crystal with dimensions of about 3 × 3 × 2 mm^3 was checked by x-ray Laue diffraction.

The temperature and magnetic field variations of the neutron diffraction intensities shown in Fig. 2, Fig. S3, and Figs. S5 and S6 were measured for $SrFeO_3$ with a cold neutron time-of-flight diffractometer, WISH (Wide angle In a Single Histogram) [41, 42], at the ISIS Facility in UK. The single crystal $SrFeO_3$ was loaded into a vertical-field cryomagnet, whose maximum field is 13.5 T. The cubic [111] axis was set to be parallel to the magnetic field. The cryomagnet has a large vertical opening angle from -5° to 10°, which enabled us to measure the out-of-plane incommensurate magnetic reflections around the reciprocal lattice point of (1, $\bar{1}$, 0) (Figs. 2 and S3) as well as that of (0, 0, 0) (Figs. S5 and S6) under magnetic field along the [111] direction [42].

Small angle neutron scattering (SANS) measurements were carried out for $SrFe_{0.99}Co_{0.01}O_3$ with a vertical-field cryomagnet (7 T in maximum) at the cold diffractometer MIRA at FRM II [43, 44], and a horizontal-field cryomagnet (6.8 T in maximum) at the SANS-I instrument at the Swiss spallation neutron source SINQ, Paul Scherrer Institute, Villigen, Switzerland. We employed an experimental setup of the horizontal configuration (see Fig. S1(a)), in which the sample can be rotated by 360° around the [$\bar{1}\bar{1}2$] axis (ω axis), and vertical configuration (see Fig. S1(b)), in which the sample can be rotated by 360 around the [111] axis (ω axis) [42]. In both experimental configurations, magnetic field was applied parallel to the [111] axis and perpendicular to the incident neutron beam. Experimental data taken at MIRA were collected both in polarized and unpolarized modes at a wavelength λ = 4.5 Å, and those at SANS-I were collected in unpolarized mode at λ = 4.7 Å. For the SANS experiments, we used $SrFe_{0.99}Co_{0.01}O_3$ instead of $SrFeO_3$, because $SrFe_{0.99}Co_{0.01}O_3$ exhibits the same magnetic phases as $SrFeO_3$ but is more suitable for studying the II-V phase transition by the SANS diffractometer equipped with a spin analyzer and a cryomagnet of 7 T, since its transition field is reduced below 7 T. The observed magnetic reflections are located around the reciprocal lattice point of (0, 0, 0). Background of each dataset was determined at high temperatures above 135 K and accordingly subtracted. The polarization of neutron spins was generated by the magnetic field gradient near the vertical superconducting magnet. The neutron flipping ratios F for the measurements at 0.3 T and 7 T are 4.9 and 3.0, respectively. Here, F is related to the neutron polarization P_n by $F = (1 + P_\mathrm{n})/(1 - P_\mathrm{n})$.

III. RESULTS AND DISCUSSION

A. Multiple-q helimagnetic spin structures

Figures 1(b) and 1(c) illustrate the spin structures reproduced by the superposition of the double-$\boldsymbol{q}$ and quadruple-$\boldsymbol{q}$ magnetic modulations, which we propose in this study as models for Phases I and II, respectively. Note that we tentatively adopt the same helicity and phase for each spin modulation. Owing to the cubic symmetry of the crystal, there are four $\boldsymbol{q}$-vectors of (q, q, q), $(-q, -q, q)$, $(-q, q, -q)$ and $(q, -q, -q)$; in this paper, we refer to them as $\boldsymbol{q}_1$, $\boldsymbol{q}_2$, $\boldsymbol{q}_3$, and $\boldsymbol{q}_4$, respectively, as described in Fig. 1(a). As explained later in detail, Phase I can be described as a double-$\boldsymbol{q}$ structure encompassing proper-screw and cycloidal modulations with slightly different $\boldsymbol{q}$-vectors, so that the overall symmetry of the superstructure is reduced [42]. As shown in Fig. 1(b), there exist singularities indicated by the blue and red circles surrounded by noncoplanar vortex-like spin configurations. On the other hand for Phase II, four equivalent proper-screw-type spin modulations yield a face-centered cubic lattice of topological singularities, at which the hedgehog/anti-hedgehog spin texture acts as the source/sink of the emergent magnetic fields (Fig. 1(c)), i.e., an emergent magnetic monopole/antimonopole. Considering the theoretical calculations in Ref. [45], the observation of the topological Hall effect in Phase II is consistent with the emergence of this three-dimensional topological spin texture [22]. Here we define the topological number as the integral of the solid angle made by the three adjacent spins around the singular point as described in Refs. [4, 45]. Following this definition, the local topological numbers for the hedgehog and antihedgehog spin textures in Phase II are 1 and -1, respectively, whereas that for the singularities in Phase I is not a non-zero integer. Thus, while the spin texture in Phase II is topological, that in Phase I might not be topological.

B. Temperature dependence of the magnetic scattering intensity

First, let us identify the multiple-$\boldsymbol{q}$ state in Phases I and II on the basis of results of high-resolution neutron diffraction measurements for $\mathrm{SrFeO_3}$ at the WISH (Wide angle In a Single Histogram) diffractometer in ISIS. Figure 2(a) shows integrated intensities of incommensurate magnetic reflections around the $(1, \bar{1}, 0)$ reciprocal lattice point, which were measured on heating in zero field after field cooling (FC) with an external field $\boldsymbol{H}$ of 7 T along the [111] axis. The data labeled $\boldsymbol{q}_i$ show the intensity corresponding to the magnetic modulation vector $\boldsymbol{q}_i$. We found that the intensity for the modulation vector of $\boldsymbol{q}_1$ at zero field was largely enhanced after the FC process with H parallel to $\boldsymbol{q}_1$ as shown in Fig. 2(a). This tendency is reminiscent of a proper-screw type magnetic order, in which a $\boldsymbol{q}$ vector parallel to $\boldsymbol{H}$ would be selected through the FC process due to the difference in the Zeeman energy. This is also consistent with the early neutron diffraction study proposing a simple screw-type structure [32]. However, nonzero scattering intensities are found not only for $\boldsymbol{q}_1$ but for $\boldsymbol{q}_{2-4}$. Thus, the possibility of the single-$\boldsymbol{q}$ proper-screw spin structure can be ruled out for Phase I and likewise for Phase II. These results suggest that the magnetic structure of Phase I is a multiple-$\boldsymbol{q}$ structure having at least two magnetic modulations; the major component with a proper-screw-like modulation ($\boldsymbol{q}_1$) and additional modulations ($\boldsymbol{q}_{2-4}$). Importantly, for Phase I, the intensities of the reflections corresponding to $\boldsymbol{q}_2$, $\boldsymbol{q}_3$ and $\boldsymbol{q}_4$ can be different from each other not only after the zero-field-cooling (ZFC) process but after the FC process (see Fig. S2 for details [42]). In other words, the threefold rotational symmetry about the [111] axis is absent in Phase I, reflecting the anisotropic magnetic structure allowing multi-domain states under an external field along [111]. Therefore, we propose that Phase I has the anisotropic double-$\boldsymbol{q}$ spin structure consisting of two kinds of magnetic modulations, one of which is proper-screw type. On the other hand for Phase II, the scattering intensities are comparable to each other, suggesting that the field-oriented anisotropic magnetic structure in Phase I disappears upon the first-order phase transition to Phase II.

C. Field dependence of the magnetic scattering intensity in Phases I and II

Having confirmed the multiple-$\boldsymbol{q}$ state in Phases I and II, we measured the intensities of the incommensurate magnetic reflections around (1,-1,0) reciprocal lattice point with varying magnetic field at the selected temperatures after zero-field cooling (ZFC) as shown in Figs. 2(b) and 2(c) (for the raw data, see Fig. S3 [42]). At 50 K and zero field in Phase I, the scattering intensities for $\boldsymbol{q}_{1-4}$ are distributed in a certain range, reflecting the multidomain state of the anisotropic multiple-$\boldsymbol{q}$ spin structure. As H is increased beyond 5 T, the intensity only for $\boldsymbol{q}_1$ parallel to $\boldsymbol{H}$ becomes larger, and the others become smaller. The significant H-induced change with a large hysteresis at low H is ascribable to the domain reorientation, as also suggested by the previous report on the magnetoresistance anomaly measured after ZFC (see the shaded area in Figs. 1(a) and 2(b)) [36]. Here, we would like to emphasize that the intensities for $\boldsymbol{q}_{2-4}$ never disappeared even in a magnetic field of 12 T. This is another evidence for the anisotropic double-$\boldsymbol{q}$ magnetic structure in Phase I. For Phase II, on the other hand, the scattering intensities for $\boldsymbol{q}_{1-4}$ are comparable to each other and H-dependent anomalies and hysteresis are absent (see Fig. 2(c)), being consistent with the presumed isotropic quadruple-$\boldsymbol{q}$ helimagnetic structure. Upon an increase in H to 12 T that induces the II-IV phase transition, the intensity distribution tends to become the one expected for the single-$\boldsymbol{q}$ state. However, since the maximum H of 12 T is located near the phase boundary and the scattering intensities for $\boldsymbol{q}_{2-4}$ remain nonzero, further experiments with larger H are indispensable to characterize the spin structure of Phase IV.

D. Direction of the helimagnetic $\boldsymbol{q}$ vectors in Phases I and II

To further characterize the multiple-$\boldsymbol{q}$ spin structure and the domain state in Phase I, we measured small-angle neutron scattering (SANS) for $\boldsymbol{q}_1$ and $\boldsymbol{q}_2$ after FC and ZFC. The SANS experiments were performed for $\mathrm{SrFe_{0.99}Co_{0.01}O_3}$ having essentially the same phase diagram as $\mathrm{SrFeO_3}$ (see Fig. 4(a)) [46], while the magnitude of the $\boldsymbol{q}$ vectors of $\mathrm{SrFe_{0.99}Co_{0.01}O_3}$ are about 8 % smaller than that of $\mathrm{SrFeO_3}$. Figure 3(e) shows the magnetic reflections around $\boldsymbol{q}_1$ as functions of and measured at 3 K after FC. Here, and correspond to the relative angles from [111] to vertical and horizontal directions, respectively, in the horizontal configuration [see Fig. 3(a)]. The intensity of the profile at selected and is obtained by the integration as a function of the momentum transfer vector $\boldsymbol{Q}$ in a range, $0.28 \leq |\boldsymbol{Q}| \leq 0.38$ (For detail, see Fig. S4 [42]). The scattering profile for $\boldsymbol{q}_1$ revealed that the magnetic modulation wave vector is no longer described by the simple (q, q, q), but split into three peaks indexed as (q, q, q') $(= \boldsymbol{q}'_{1(2)})$, (q, q', q) $(= \boldsymbol{q}'_{1(3)})$ and (q', q, q) $(= \boldsymbol{q}'_{1(4)})$, where $q \simeq 0.114$ [r. l. u.] and $q' \simeq 0.123$ [r. l. u.]. The observation of the triplet peaks around $\boldsymbol{q}_1$ after FC with $\boldsymbol{H}$ parallel to [111] is a signature of the three $\boldsymbol{q}$-dependent domains (for detail, see Fig. S2 [42]). On the other hand for $\boldsymbol{q}_2$ in Fig. 3(g), a single peak is found at the position slightly shifted from the $[\bar{1}\bar{1}1]$ direction, which is assigned as $(-q, -q, q')$ $(= \boldsymbol{q}'_{2(1)})$. The azimuthal directions of these propagation vectors deviate from the <111> equivalents, so that the double-$\boldsymbol{q}$ state in Phase I can accommodate the angular mismatch between the two $\boldsymbol{q}$ vectors. As the temperature increases through the I-II phase transition at 90 K, the directions of all propagation vectors become parallel to the <111> equivalents, consistent with the proposal for the isotropic quadruple-$\boldsymbol{q}$ helmagnetic structure in Phase II (see Figs. 3(d), (f), and (h)). The schematic representations of the observed scattering peaks for Phases I and II are displayed in Figs. 3(c) and 3(d), respectively. The numbers of the domain types of Phase I after ZFC and FC states are 12 and 3, respectively, the latter of which is obtained by considering the three-fold symmetry around [111] (We ignored the helicity degree of freedom for the consideration of the domain types.). At least at low temperature, magnetic fields of order ∼10 T therefore mostly select different equivalent domains without modifying the magnetic structure substantially. In contrast to the present system showing distinct $\boldsymbol{q}$-dependent domains, helimagnetic $\boldsymbol{q}$-vectors in MnSi can be continuously reoriented towards the field direction by small magnetic fields of 0.1 T [47], which presumably reflects the difference in the magnetic anisotropy or the helimagnetic period (18 nm for MnSi and 1.8 nm for $SrFeO_3$).

E. Polarized small angle neutron scattering

Next, we performed polarized SANS experiments to learn microscopically how the spins are modulating along $\boldsymbol{q}_2'$ or $\boldsymbol{q}_2$ after the FC process with $\boldsymbol{H}$ along [111]. Here, we assume three possible arrangements of spin modulation: i) vertical-cycloid (-sinusoidal) type with spins on the plane parallel to $\boldsymbol{q}_2'$ and $\boldsymbol{H}$ (Fig. 4(d)); ii) proper-screw type with spins on the plane normal to $\boldsymbol{q}_2$ (Fig. 4(e)); and iii) horizontal-cycloid (-sinusoidal) type with spins on the plane parallel to $\boldsymbol{q}_2$ and normal to $\boldsymbol{H}$ (Fig. 4(f)). Since only the component of the magnetic moments perpendicular to the scattering vector causes neutron scattering, the spin components contributing to the scattering intensity can be described as shown at the right end of Figs. 4(d-f). In the polarized SANS measurements, since the non-spin-flip (NSF) and the spin-flip (SF) geometries detect only the spin components parallel and normal to $\boldsymbol{H}$, respectively, the intensity ratios of NSF and SF scattering at $\boldsymbol{q}_2'$ or $\boldsymbol{q}_2$ are expected to display the dependence represented by the relative lengths of the blue and red arrows in Figs. 4(d-f). From the intensity ratios, we can distinguish between the three types of spin spirals shown at the left side of Figs. 4(d-f), while we cannot rule out the possibility that the sinusoidal spin modulations shown at the right side of Figs. 4(d) and 4(f) are more proper models. The measurements were performed after FC in Phase I, so that 3 kinds of domains with $\boldsymbol{q}_1'$

nearly parallel to $\boldsymbol{H}$ are selected. The inset of Fig. 4(a) shows the ω-scan profiles of the magnetic scattering for $\boldsymbol{q}_2'$ at 3 K and 0.3 T, which were normalized by the flipping ratios. As shown in Figs. 4(b) and 4(c), the normalized scattering intensity for the NSF geometry is much larger than that for the SF geometry in Phase I, whereas the scattering intensities for both geometries are nearly the same in Phase II. This result indicates that Phase I and Phase II encompass vertical-cycloid and proper-screw states, respectively, propagating along $[\bar{1}\bar{1}1]$, being consistent with the fact that the magnetic scattering intensity along [111] is much larger than those along the other <111> equivalents after FC in Phase I, which is not the case for Phase II (see Fig. 2(a)). In Phase V at 7 T, the scattering intensity for the SF geometry is larger than that for the NSF geometry, implying that the spin arrangement propagating along $[\bar{1}\bar{1}1]$ is in the horizontal-cycloid type (see Fig. 4(f)). To be noted here is that each multiple-$\boldsymbol{q}$ spin spiral is expected to have a ferromagnetic component induced by external magnetic fields, which cannot be confirmed in this work. Thus, it is presumable that Phase V has multiple-$\boldsymbol{q}$ spin spirals as well, but calling for further experiments to identify the detailed spin structure.

IV. CONCLUSIONS

To summarize, we have identified two kinds of multiple-$\boldsymbol{q}$ spin structures in $SrFeO_3$, that appear robustly even without external magnetic fields. The anisotropic double-$\boldsymbol{q}$ spin structure in Phase I manifests itself as a nontrivial order reflecting the versatility of the centrosymmetric lattice that permits various types of spin spiral. However, this spin texture cannot explain the observed topological Hall resistivity, because the expected direction of the emergent magnetic flux is perpendicular to the external magnetic field. Future research will have to assess whether the discrepancy between the expected and observed directions of the emergent magnetic flux in Phase I arises from an additional internal spin modulation that is not resolved in the current experiment. On the other hand, Phase II can be described in terms of a topologically nontrivial order with an isotropic quadruple-$\boldsymbol{q}$ spin spiral, that presumably yields emergent magnetic monopoles as reported for the noncentrosymmetric helimagnet MnGe characterized by an orthogonal triple-$\boldsymbol{q}$ spiral [21].

We now turn to the mechanisms underlying the observed cascade of magnetic phase transitions. The fact that the diffraction patterns at the lowest temperature in ZFC and FC states are closely similar implies that Phase I is not stabilized by the Zeeman interaction, but rather by anisotropic terms in the zero-field spin Hamiltonian (such as magneto-crystalline anisotropies generated by the spin-orbit coupling) that go beyond the primary isotropic double-exchange and/or superexchange interactions. With increasing temperature, the corresponding free-energy gain could be offset by the higher entropy of the more symmetric quadruple-$\boldsymbol{q}$ structure, leading to the observed phase transition between Phases I and II. Recently, Monte Carlo simulations based on a Kondo lattice model with a biquadratic interaction defined in momentum space have indicated various multiple-$\boldsymbol{q}$ phases on a centrosymmetric lattice with rotational symmetry[28]. Although this model does not apply directly to our system, this theoretical work and our experimental results provide a timely showcase of the rich variety of multiple-$\boldsymbol{q}$ helimagnetic phases with topological singularities that can be expected to emerge ubiquitously in frustrated itinerant magnets with high lattice symmetry, even without the DM interaction. Moreover, perovskite-type oxides are a broad class of materials that already find many applications especially in the form of heterostructures enabling the interplay between topological magnetism and other collective quantum phenomena. The discovery of topological spin order in $SrFeO_3$ is therefore a milestone for integrating potential topological magnetic states into existing device architectures.

References

[1] A. Bogdanov and A. Hubert, Thermodynamically stable magnetic vortex states in magnetic crystals. J. Magn. Magn. Mater. **138**, 255-269 (1994).

[2] U. K. Rößler, A. N. Bogdanov, and C. Pfleiderer, Spontaneous skyrmion ground states in magnetic metals. Nature (London) **442**, 797-801 (2006).

[3] S. Mühlbauer, B. Binz, F. Jonietz, C. Pfleiderer, A. Rosch, A. Neubauer, R. Georgii, P. Böni, Skyrmion lattice in a chiral magnet. Science **323**, 915-919 (2009).

[4] N. Nagaosa, Y. Tokura, Topological properties and dynamics of magnetic skyrmions. Nat. Nanotechnol. **8**, 899-911 (2013).

[5] N. Kanazawa, S. Seki, Y. Tokura, Noncentrosymmetric magnets hosting magnetic skyrmions. Adv. Mater. **29**, 1603227 (2017).

[6] A. Neubauer, C. Pfleiderer, B. Binz, A. Rosch, R. Ritz, P. G. Niklowitz, and P. Böni, Topological Hall Effect in the *A* Phase of MnSi. Phys. Rev. Lett. **102**, 186602 (2009).

[7] N. Kanazawa, Y. Onose, T. Arima, D. Okuyama, K. Ohoyama, S. Wakimoto, K. Kakurai, S. Ishiwata, and Y. Tokura, Large Topological Hall Effect in a Short-Period Helimagnet MnGe. Phys. Rev. Lett. **106**, 156603 (2011).

[8] F. Jonietz, S. Mühlbauer, C. Pfleiderer, A. Neubauer, W. Münzer, A. Bauer, T. Adams, R. Georgii, P. Böni, R. A. Duine, K. Everschor, M. Garst, A. Rosch, Spin Transfer Torques in MnSi at Ultralow Current Densities. Science **330**, 1648-1651 (2010).

[9] M. Mochizuki, X. Z. Yu, S. Seki, N. Kanazawa, W. Koshibae, J. Zang, M. Mostovoy, Y. Tokura and N. Nagaosa, Thermally driven ratchet motion of a skyrmion microcrystal and topological magnon Hall effect. Nat. Mater. **13**, 241-246 (2014).

[10] X. Z. Yu, Y. Onose, N. Kanazawa, J. H. Park, J. H. Han, Y. Matsui, N. Nagaosa, and Y. Tokura, Real-space observation of a two-dimensional skyrmion crystal. Nature (London) **465**, 901-904 (2010).

[11] W. Münzer, A. Neubauer, T. Adams, S. Mühlbauer, C. Franz, F. Jonietz, R. Georgii, P. Böni, B. Pedersen, M. Schmidt, A. Rosch, and C. Pfleiderer, Skyrmion lattice in the doped semiconductor $\mathrm{Fe}_{1-x}\mathrm{Co}_x\mathrm{Si}$. Phys. Rev. B **81**, 041203(R) (2010).

[12] X. Z. Yu, N. Kanazawa, Y. Onose, K. Kimoto, W. Z. Zhang, S. Ishiwata, Y. Matsui and Y. Tokura, Near room-temperature formation of a skyrmion crystal in thin-films of the helimagnet FeGe. Nat. Mater. **10**, 106-109 (2011).

[13] S. Seki, X. Z. Yu, S. Ishiwata, Y. Tokura, Observation of skyrmions in a multiferroic material. Science **336**, 198-201 (2012).

[14] Y. Tokunaga et al., A new class of chiral materials hosting magnetic skyrmions beyond room temperature. Nat. Commun. **6**, 7638 (2015).

[15] I. Kézsmárki, S. Bordács, P. Milde, E. Neuber, L. M. Eng, J. S. White, H. M. Ronnow, C. D. Dewhurst, M. Mochizuki, K. Yanai, H. Nakamura, D. Ehlers, V. Tsurkan, A. Loidl, Néel-type skyrmion lattice with confined orientation in the polar magnetic semiconductor $\mathrm{GaV}_4\mathrm{S}_8$. Nat. Mater. **14**, 1116-1122 (2015).

[16] Y. Fujima, N. Abe, Y. Tokunaga, T. Arima, Thermodynamically stable skyrmion lattice at low temperatures in a bulk crystal of lacunar spinel $\mathrm{GaV}_4\mathrm{Se}_8$. Phys. Rev. B **95**, 180410(R) (2017).

[17] S. Bordács, A. Butykai, B. G. Szigeti, J. S. White, R. Cubitt, A. O. Leonov, S. Widmann, D. Ehlers, H.-A. Krug von Nidda, V. Tsurkan, A. Loidl, I. Kézsmárki Equilibrium Skyrmion Lattice Ground State in a Polar Easy-plane Magnet. Sci. Rep. **7**, 7584 (2017).

[18] T. Kurumaji, T. Nakajima, V. Ukleev, A. Feoktystov, T. Arima, K. Kakurai, and Y. Tokura, Néel-type skyrmion lattice with confined orientation in the polar magnetic semiconductor Phys. Rev. Lett. **119**, 237201 (2017).

[19] A. K. Nayak, V. Kumar, T. Ma, P. Werner, E. Pippel, R. Sahoo, F. Damay, U. K. Rößler, C. Felser, S. S. P. Parkin, Magnetic antiskyrmions above room temperature in tetragonal Heusler materials. Nature **548**, 561 (2017).

[20] S. Heinze, K. von Bergmann, M. Menzel, J. Brede, A. Kubetzka, R. Wiesendanger, G. Bihlmayer, S. Blügel, Spontaneous atomic-scale magnetic skyrmion lattice in two dimensions. Nat. Phys. **7**, 713 (2011).

[21] N. Kanazawa, J.-H. Kim, D. S. Inosov, J. S. White, N. Egetenmeyer, J. L. Gavilano, S. Ishiwata, Y. Onose, T. Arima, B. Keimer, and Y. Tokura, Possible skyrmion-lattice ground state in the B20 chiral-lattice magnet MnGe as seen via small-angle neutron scattering. Phys. Rev. B **86**, 134425 (2012).

[22] N. Kanazawa, Y. Nii, X. -X. Zhang, A. S. Mishchenko, G. De Filippis, F. Kagawa, Y. Iwasa, N. Nagaosa and Y. Tokura, Critical phenomena of emergent magnetic monopoles in a chiral magnet. Nat. Commun. **7**, 11622 (2016).

[23] T. Okubo, S. Chung, and H. Kawamura, Multiple-q states and the skyrmion lattice of the triangular-lattice Heisenberg antiferromagnet under magnetic fields. Phys. Rev. Lett. **108**, 017206 (2012).

[24] A. O. Leonov and M. Mostovoy, Multiply periodic states and isolated skyrmions in an anisotropic frustrated magnet. Nat. Commun. **6**, 8275 (2015).

[25] Z. Wang, Y. Kamiya, A. H. Nevidomskyy, and C. D. Batista, Three-Dimensional Crystallization of Vortex Strings in Frustrated Quantum Magnets. Phys. Rev. Lett. **115**, 107201 (2015).

[26] C. D. Batista, S. -Z. Lin, S. Hayami, and Y. Kamiya, Frustration and chiral orderings in correlated electron systems. Rep. Prog. Phys. **79**, 084504 (2016).

[27] R. Ozawa, S. Hayami, K. Barros, G. -W. Chern, Y. Motome, and C. D. Batista, Vortex Crystals with Chiral Stripes in Itinerant Magnets. J. Phys. Soc. Jpn. **85**, 103703 (2016)

[28] S. Hayami, R. Ozawa, and Y. Motome, Effective bilinear-biquadratic model for noncoplanar ordering in itinerant magnets. Phys. Rev. B **95**, 224424 (2017).

[29] E. M. Forgan, E. P. Gibbons, K. A. McEwen, and D. Fort, Observation of a Quadruple-q Magnetic Structure in Neodymium. Phys. Rev. Lett. **62**, 470 (1989).

[30] J. Jensen and A. R. Mackintosh, Rare Earth Magnetism; Structures and Excitations. Oxford University Press, Oxford (1991).

[31] J. B. MacChesney, R. C. Sherwood, and J. F. Potter, Electric and Magnetic Properties of the Strontium Ferrates. J. Chem. Phys. **43**, 1907 (1965).

[32] T. Takeda, Y. Yamaguchi, and H. Watanabe, Magnetic structure of $SrFeO_3$. J. Phys. Soc. Jpn. **33**, 967 (1972).

[33] J. -H. Kim, A. Jain, M. Reehuis, G. Khaliullin, D. C. Peets, C. Ulrich, J. T. Park, E. Faulhaber, A. Hoser, H. C. Walker, D. T. Adroja, A. C. Walters, D. S. Inosov, A. Maljuk, and B. Keimer, Competing Exchange Interactions on the Verge of a Metal-Insulator Transition in the Two-Dimensional Spiral Magnet $Sr_3Fe_2O_7$. Phys. Rev. Lett. **113**, 147206 (2014)

[34] M. Mostovoy, Helicoidal Ordering in Iron Perovskites. Phys. Rev. Lett. **94**, 137205 (2005).

[35] M. Azhar and M. Mostovoy, Incommensurate Spiral Order from Double-Exchange Interactions. Phys. Rev. Lett. **118**, 027203 (2017).

[36] S. Ishiwata, M. Tokunaga, Y. Kaneko, D. Okuyama, Y. Tokunaga, S. Wakimoto, K. Kakurai, T. Arima, Y. Taguchi, and Y. Tokura, Versatile helimagnetic phases under magnetic fields in cubic perovskite $SrFeO_3$. Phys. Rev. B. **84**, 054427 (2011).

[37] M. Reehuis, C. Ulrich, A. Maljuk, Ch. Niedermayer, B. Ouladdiaf, A. Hoser, T. Hofmann, and B. Keimer, Neutron diffraction study of spin and charge ordering in $SrFeO_{3-\delta}$. Phys. Rev. B. **85**, 184109 (2012).

[38] N. Hayashi, T. Terashima, and M. Takano, Oxygen-holes creating different electronic phases in Fe^{4+}-oxides: successful growth of single crystalline films of $SrFeO_3$ and related perovskites at low oxygen pressure. J. Mater. Chem. **11**, 2235 (2001).

[39] S. Chakraverty, T. Matsuda, H. Wadati, J. Okamoto, Y. Yamasaki, H. Nakao, Y. Murakami, S. Ishiwata, M. Kawasaki,Y. Taguchi, Y. Tokura, and H. Y. Hwang, Multiple helimagnetic phases and topological Hall effect in epitaxial thin films of pristine and Co-doped $\mathrm{SrFeO_3}$. Phys. Rev. B **88**, 220405(R) (2013).

[40] Y. W. Long, Y. Kaneko, S. Ishiwata, Y. Taguchi, and Y. Tokura, Synthesis of cubic $\mathrm{SrCoO_3}$ single crystal and its anisotropic magnetic and transport properties. J. Phys.: Condens. Matter **23**, 245601 (2011).

[41] L. C. Chapon, P. Manuel, P. G. Radaelli, C. Benson, L. Perrott, S. Ansell, N. J. Rhodes, D. Raspino, D. Duxbury, E. Spill, and J. Norris, Wish: the new powder and single crystal magnetic diffractometer on the second target station. Neutron News **22**, 22 (2011).

[42] See Supplemental Material at [URL will be inserted by publisher] for details on neutron measurements and the domain state of double-$\boldsymbol{q}$ helimagnetic structure in Phase I. In addition, raw data of WISH experiments and SANS experiments are shown.

[43] R. Georgii and K. Seemann, MIRA: Dual wavelength band instrument. Journal of large-scale research facilities **1**, A3 (2015).

[44] R. Georgii, T. Weber, G. Brandl, M. Skoulatos, M. Janoschek, S. Mühlbauer, C. Pfleiderer, P. Böni, The multi-purpose three-axis spectrometer (TAS) MIRA at FRM II. Nuclear Instruments and Methods in Physics Research Section A **881**, 60 (2018).

[45] J. H. Park and J. H. Han, Zero-temperature phases for chiral magnets in three dimensions. Phys. Rev. B **83**, 184406 (2011).

[46] Y. W. Long, Y. Kaneko, S. Ishiwata, Y. Tokunaga, T. Matsuda, H. Wadati, Y. Tanaka, S. Shin, Y. Tokura, and Y. Taguchi, Evolution of magnetic phases in single crystals of $\mathrm{SrFe_{1-x}Co_xO_3}$ solid solution. Phys. Rev. B **86**, 064436 (2012).

[47] A. Bauer, A. Chacon, M. Wagner, M. Halder, R. Georgii, A. Rosch, C. Pfleiderer, and M. Garst, Symmetry breaking, slow relaxation dynamics,

and topological defects at the field-induced helix reorientation in MnSi. Phys. Rev. B **95**, 024429 (2017).

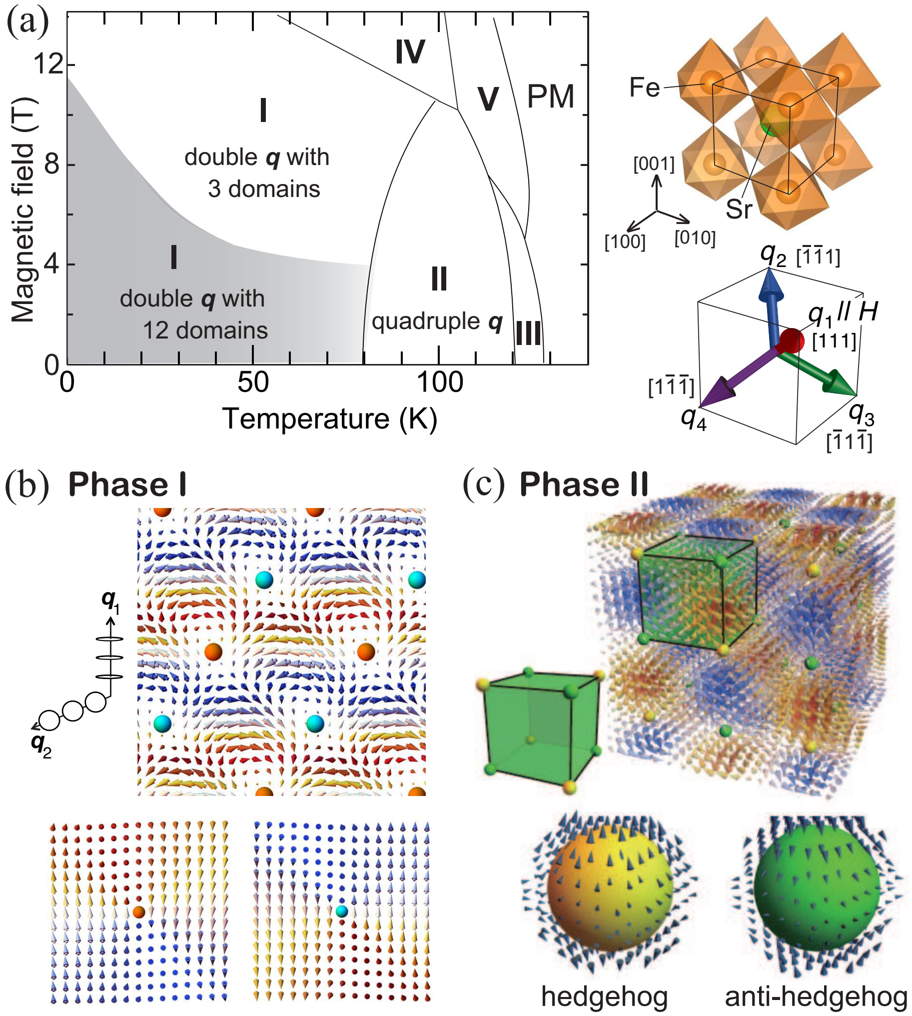

FIG. 1: (a) Magnetic phase diagram for the applied field direction along [111]. The shaded and the white regions in Phase I correspond to states with 12 and 3 domains, respectively. Schematic crystal structure and quadruple-$\boldsymbol{q}$ vectors viewed along [111] are shown on the righthand side. (b) Double-$\boldsymbol{q}$ spin structure in Phase I and (c) quadruple-$\boldsymbol{q}$ spin structure in Phase II (the color of each spin corresponds to the spin component along the direction perpendicular to both $\boldsymbol{q}_1$ and $\boldsymbol{q}_2$ for panel (b) and that along [111] for panel (c), respectively). The magnified views around the singular points are shown at the bottom. Note that we adopt $\boldsymbol{q}_1$ and $\boldsymbol{q}_2$ instead of $\boldsymbol{q}'_1$ and $\boldsymbol{q}'_2$ for Phase I.

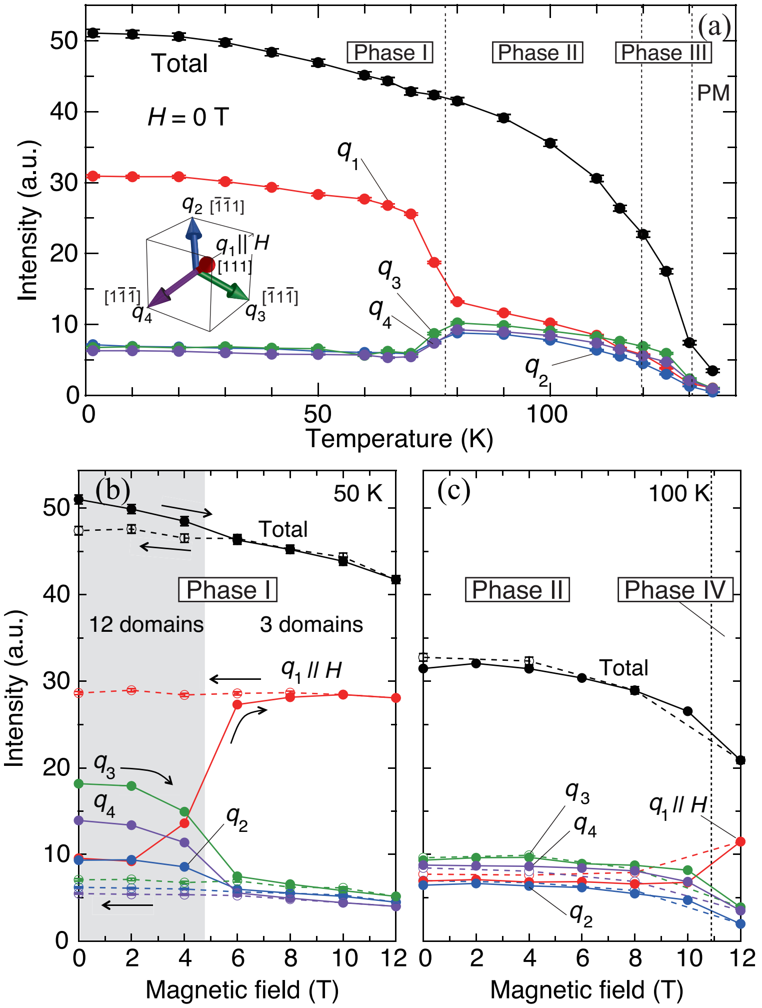

FIG. 2: (a) Temperature dependence of integrated intensities of the magnetic scattering along $\boldsymbol{q}_i$ ($i = 1-4$) measured at zero field after field cooling. The total intensity for $\boldsymbol{q}_{1-4}$ is also shown. Magnetic field dependence of the magnetic scattering intensities for (b) Phase I at 50 K and (c) Phase II at 100 K. The data with solid lines and broken lines were measured on increasing and decreasing the field along [111], respectively. All the data were measured after zero-field cooling from room temperature.

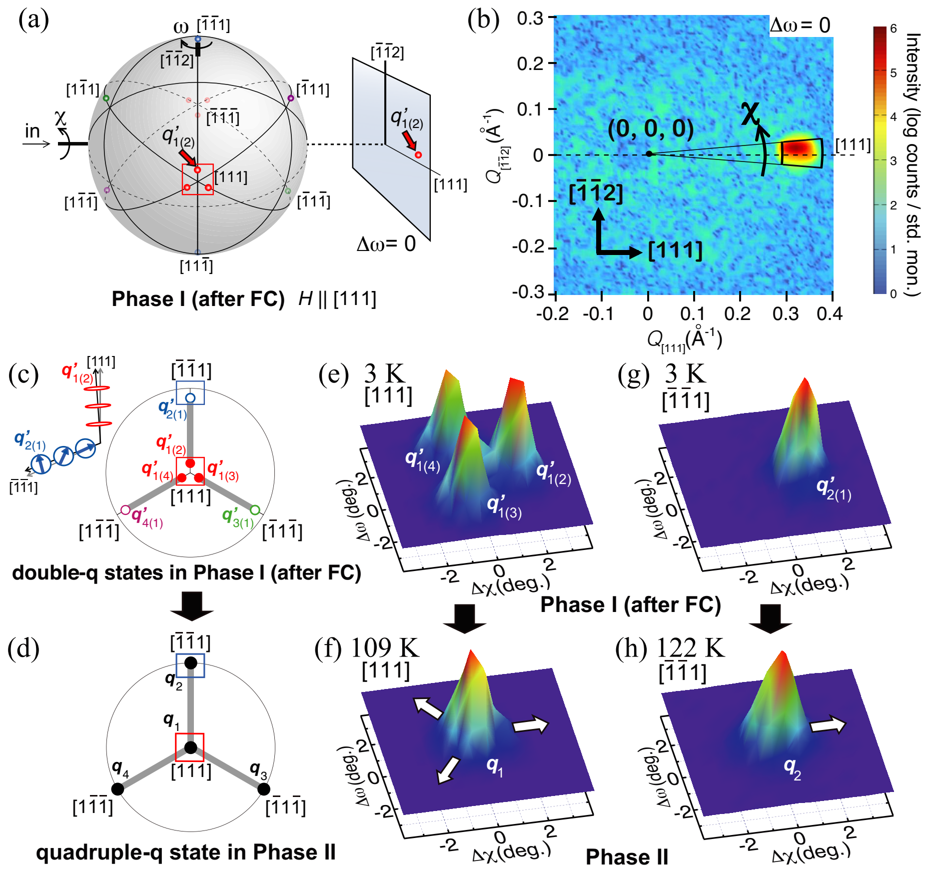

FIG. 3: (a) Schematic representation describing the crystallographic directions and the azimuthal positions of magnetic scattering peaks in the horizontal configuration for Phase I after field cooling (FC). The three red balls indicated by the red square on the gray sphere correspond to the triplet magnetic scattering peaks deviated by 2°) from the [111] direction. (b) SANS data measured at 3 K with the relative rocking angle $\Delta\omega = 0$. The observed magnetic reflection corresponds to the helimagnetic modulation $\boldsymbol{q}'_{1(2)}$, which is indicated by the red arrow in the panel (a). Stereographic projections of magnetic scattering peaks in Phase I after field cooling (c) and Phase II (d). The filled and open circles represent the magnetic reflections for the proper-screw and the vertical-cycloid-type spin propagation, respectively. (e,f) Integrated magnetic scattering profiles around $\boldsymbol{q}_1$ parallel to [111]. The peaks in panels (e) and (g) correspond to the triplet red filled circles and a single blue open circle in the panel (c), respectively. (g,h) Integrated magnetic scattering profiles around $\boldsymbol{q}_2$ parallel to [$\bar{1}\bar{1}1$]. The intensity is normalized by the largest value. The data were collected on heating in zero field after field cooling under a magnetic field of 6.8 T for $\mathrm{SrFe_{0.99}Co_{0.01}O_3}$. The data in panels (b), (e), and (f) were collected with the horizontal configuration, and those in panels (g) and (h) were collected with the vertical configuration (See Fig. S1 [?]).

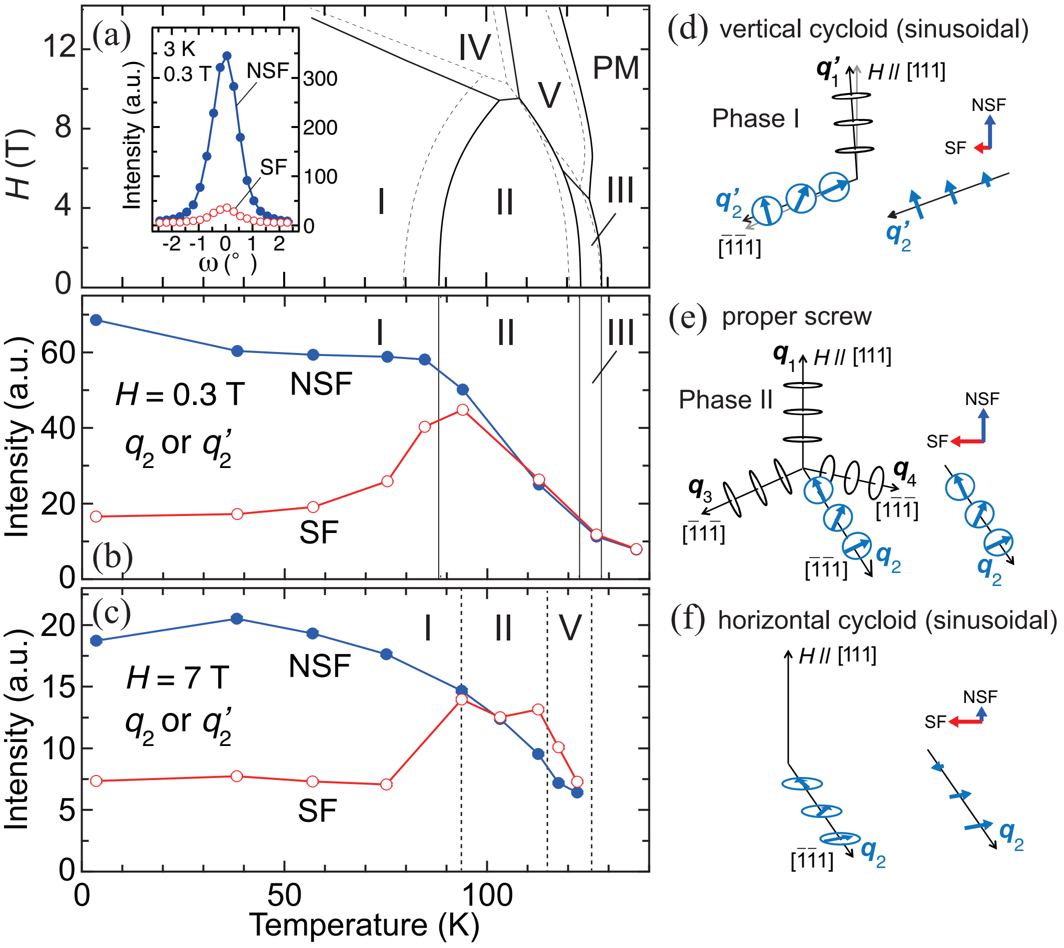

FIG. 4: (a) The magnetic phase diagram of $SrFe_{0.99}Co_{0.01}O_3$ reproduced from [46], on which the magnetic phase diagram of $SrFeO_3$ is superimposed (the phase boundary of $SrFeO_3$ is shown by broken lines). The integrated neutron scattering intensities as a function of $\Delta\omega$ at 3 K and 0.3 T for spin flip (SF) and non spin flip (NSF) geometries are shown as an inset. All the data were collected after field cooling in a magnetic field of 7 T. Temperature dependence of SF and NSF scattering intensities measured on heating at (b) 0.3 T and (c) 7 T. In each case, the applied magnetic field and the incident neutron spin are parallel to [111]. Schematic illustrations of the spiral spin propagation for $\boldsymbol{q}_2'$ or $\boldsymbol{q}_2$ with (d) vertical-cycloid-type (Phase I), (e) proper-screw-type (Phase II), and (f) horizontal-cycloid-type configurations, the right-hand side of which shows the effective spin components for spin-polarized SANS.

Acknowledgments

The authors thank M. Mostovoy, S. Hayami, Y. Motome, N. Nagaosa, and M. Takano for useful comments, and thank N. Egetenmeyer for her kind experimental support. This work is partly supported by Grant-in-Aid for Scientific Research, Japan Society for the Promotion of Science, Japan (Kakenhi No. 17H01195 and No. 16K17736), JST PRESTO Hyper-nano-space design toward Innovative Functionality (Grant No. JPMJPR1412), and Asahi Glass Foundation. D. S. I. acknowledges support from the German Research Foundation (DFG) through the project C03 of the Collaborative Research Center SFB 1143 in Dresden (project i.d. 247310070) and the W*ü*rzburg-Dresden Cluster of Excellence ”ct.qmat” (EXC 2147, project-id 39085490). J. S. W. acknowledges support from Swiss National Science Foundation (SNSF) via the Sinergia network ’NanoSkyrmionics’ (grant CRSII5-171003), and the SNSF project grant No. 153451. B.K. acknowledges support from the DFG through the Collaborative Research Center TRR80. Y. W. Long acknowledges support from the MOST-RIKEN collaboration project (Grant No. 2018YFE0103200).

Supplementary information is available in the online version of the paper.